Moore, J.R., P.R. Geimer, R. Finnegan, and J. Bodtker (2020). Geomorphology. doi: 10.1016/j.geomorph.2020.107244.

Between a beam and catenary: Influence of geometry on gravitational stresses and stability of natural rock arches

Jeffrey R. Moore*, Paul R. Geimer, Riley Finnegan, & Jackson Bodtker
University of Utah, Department of Geology and Geophysics, 115 S 1460 E, Salt Lake City, UT 84112 USA
**Corresponding author: jeff.moore@utah.edu*

Abstract

The self-weight of freestanding natural arches imparts stresses on the lintel and abutments, setting the conditions for rock fracture and erosion. Rock is weak in tension, therefore an ideal arch form is one that minimizes tensile stresses and supports the weight of the lintel in compression, e.g. an inverted catenary. However, rock mass structure, including bedding, cross-bedding and other discontinuities, often imparts strong control on the geometry of arches, leading to forms that are less favorable from a stress perspective. Here we analyze a suite of nineteen arch models created from ground- and drone-based photogrammetry to assess the three-dimensional static stress field under gravitational loading. The models represent a range of arch lengths from 4 to 88 m, as well as a variety of forms, and use material properties previously calibrated from dynamic analysis of ambient vibrations. Our results demonstrate that arches shaped like beams have relatively high tensile stresses and a nearly symmetrical statistical distribution of principal stresses, while those with convex forms have comparably lower tensile stresses and statistical distributions favoring compressive stresses. In-situ observations of tensile cracks frequently correspond to the location of predicted tensile stresses in our models. We calculated the ratio of mean principal stresses for each arch, which is theoretically 1 for a flat prismatic beam and approaches infinity for an ideal inverted catenary. We found several arches with mean principal stress ratio around 1 and that values increased with lintel convexity. These results indicate that while self-sculpture might attempt to create ideal stress-based forms, discontinuities can control lintel geometry and natural arches evolve with forms that may be less favorable for long-term stability. The mean principal stress ratio is a simple metric to classify and compare arches, useful for assessment of arch stability supporting conservation and hazard analyses.

1. Introduction

Natural arches evolve through erosion (Bruthans et al., 2014; Ostanin et al., 2017). Typically the process begins with undermining, with erosion focused at a basal weak layer or contact and progressing upwards and outwards to form an arching roof or alcove (Laity and Malin, 1985; Blair, 1987; Howard et al., 1988; Cruikshank and Aydin, 1994; Filippi et al., 2018). This erosion is facilitated by climatic and seismic forces that impart stresses on rock masses causing fracture growth and propagation (Gerber and Scheidegger, 1969; Viles, 2013; Vařilová et al., 2015; Greif et al., 2017), as well as sub-critical crack growth under static loading (Eppes and Keanini, 2017). Gravitational stresses set the conditions under which these erosional forces operate. In the absence of internal rock structure or fabric (e.g. bedding), cracks are free to grow in accordance with the stress field, e.g. under compressive loading cracks grow in the direction of maximum compressive stress and open against the minimum compressive stress (Leith et al., 2014 and references therein). However, rock masses rarely lack internal fabric, and features like bedding and cross-bedding, joints and resistant layers can play an important role in the geometrical evolution of an arch (Stevens and McCarrick, 1988). Therefore, while an arch might attempt to evolve into an ideal form in accordance with stress conditions (cf. Bruthans et al., 2014), rock mass structure commonly interrupts this process generating forms that may be less favorable for long-term stability.

Rock is weak in tension, especially over long time scales, with commonly measured tensile strengths from laboratory testing being only a fraction (roughly 1/10 to 1/100) of compressive strengths (Goodman, 1989). Therefore tensile stress conditions often limit and govern the erosional development of rock landforms, such as natural arches and towers (Řihošek et al., 2019). In civil engineering, arches can be designed to minimize tensile stresses, especially for brittle materials such as stone or brick, and arch forms have been employed by engineers for centuries for this purpose (Castigliano, 1879; i Ginovart et al., 2017). One of the best known is the inverted catenary (Heyman, 1995). A catenary curve is described by the shape of a chain hanging under its own weight – in this shape all stresses in the chain are tensile. In an inverted catenary, or arched form, all stresses are compressional and arches can be constructed from interlocking masonry relying on the high compressive strength of these materials. A parabolic form is similarly employed for bridges where the arch carries not only the weight of the lintel but also a uniform vertical load (Hibbeler, 1999). A flat fixed beam, on the other hand, will have regions of high tensile stress along the underside of the lintel and the top of the abutments, where fractures may exploit the weak tensile strength of rock to nucleate and grow, generating a potentially unstable lintel.

Natural arches exist in a variety of scales and forms and thus in a range of possible stress conditions, with some likely more favorable for long term stability than others. In one end-member case, a perfect inverted catenary, tensile stresses in the lintel are null and all stresses are compressive (Handy, 1973). In another end-member case, a flat beam, tensile and compressive principal stresses in the lintel are equal and opposite and mirrored about a horizontal axis of symmetry (Gere and Timoshenko, 1997). Due to the occurrence of tensile stresses, and the weak tensile strength of rock masses, the beam-like form is likely to be inherently less stable than the catenary form. Arch geometry may thus reflect long-term stability though the influence of form on stress. While these bounding cases represent plausible end-member stress conditions, most natural arches likely fall within the catenary-beam spectrum, with rock mass structure imparting important controls on the development of lintel geometry. For example, horizontal layering of a resistant caprock rock unit will favor development of a beam-like arch, while a massive material free of discontinuities may self-sculpt into an inverted catenary. However, to-date no comprehensive study of real arch forms exists that can be used to evaluate gravitational stress conditions and explore general relations between form and stress.

Here we test the hypothesis that natural arch geometries, and corresponding gravitational stresses, fall within end-member limits of a beam and an inverted catenary. We draw on our database of nineteen three-dimensional arch models created from ground- and drone-based photogrammetry, and use finite-element numerical analysis to estimate static stress distributions for each arch under gravitational loading. Principal stress histograms for each site allow quick cross-comparison highlighting: 1) relatively low stresses in general for actively evolving natural arches, and 2) correlation between stress distribution and arch form. Results show that several arches have stress conditions akin to a beam, while a few approach an idealized inverted catenary. We develop a summary metric, defined as the ratio of mean principal stresses (σ_1:σ_3), which we find correlates with lintel geometry and may be used to evaluate relative stress conditions in the absence of numerical analysis. Specifically, beam-like arches have mean principal stress ratios close to unity, while catenary forms have larger mean principal stress ratios (in the extreme reaching infinity as tensile stresses drop to zero). The metric allows quick comparison of forms and may be valuable for qualitative assessment of arch stability and lifespan.

2. Study Sites

Nineteen rock arches in southeastern Utah were selected for analysis in this study (Table 1, Figures 1, 2). Arch spans ranged from 4 to 88 m, and included the longest arch in North America (Landscape Arch). The features are located within national parks and monuments, and neighboring public lands (Figure 1). They occur within Jurassic sandstone units common to the Colorado Plateau: Entrada Sandstone, Navajo Sandstone, Kayenta Formation, and Wingate Sandstone, in addition to the Permian Cedar Mesa and White Rim Sandstones, and sandstone beds of the Permian Cutler and Paleogene Claron Formations (Table 1). Sites were selected based on access, simple and clear geometry, as well as cultural prominence (Figure 2). One site, Rainbow Arch, collapsed during the study period at an unknown date in the winter of 2017-18.

These features were surveyed as part of an effort to explore the resonance characteristics of natural arches (Geimer et al., 2020). For each site, field work consisted of collecting ground- and drone-based aerial imagery for creation of a 3D surface model (see Methods), as well as >1 hr ambient vibration measurements from a seismometer placed on the arch lintel. Three-dimensional finite-element modal analysis was used to recreate field vibration characteristics, resulting in a calibrated estimate of Young's modulus and confirmation of the implemented boundary conditions (Geimer et al., 2020). Density for all features was assumed to be 2000 kg/m^3 based on available laboratory data (Moore et al., 2018).

3. Methods

We generated scaled 3D models for each arch using photogrammetry. Georeferenced ground- and drone-based photos were acquired in the field covering all accessible angles of each arch, and processed using the commercial photogrammetry software ContextCapture (bentley.com). Model scaling was verified from field measurements. Surface meshes were refined in Meshmixer (meshmixer.com), including smoothing erroneous surfaces (e.g. bushes) and creation of a 3D solid for each arch. Field assessment of boundary conditions provided the basis for trimming arch abutments (Moore et al., 2018; Geimer et al., 2020). Example arch models are shown in Figure 3a,b. Two additional synthetic arch models were manually created by extruding analytical curves for an inverted catenary as well as a flat beam, with scales modeled after Rainbow Bridge and Two Bridge, respectively.

Each 3D arch model was imported into the commercial finite-element software COMSOL Multiphysics (comsol.com) (e.g. Figure 3c,d). There Geimer et al. (2020) previously performed 3D eigenfrequency analysis, implementing elastic material properties of density and Young's modulus and solving for the resonant modes. Match between resonant frequencies and

modal vectors between field data and numerical results validated the implemented geometry, material properties, and boundary conditions, demonstrating that each arch was appropriately modeled based on reproduction of measured dynamic properties. Note that not all arches included in this study were analyzed by Geimer et al. (2020) (Table 1), as at some sites (e.g. Delicate Arch) seismic data were inconclusive while other structural data were well described (in this case, the 3D model of Delicate Arch was generated from ground-based laser scanning; Shaan Hurley, personal communication). In addition, some arches in this study had adequate 3D models for stress analyses of the lintel but lacked complete coverage needed for eigenfrequency modeling (e.g. Double O Arch). We adapted the eigenfrequency models by applying gravity as a vertical body force and solving for the static stress state under self-weight loading.

Gravitational stresses in each arch model were visualized as contour surfaces (e.g. Figure 3e-h) showing the principal stress magnitudes across the exterior of each arch. The sign convention used here for all reported stresses is compression positive, tension negative, meaning σ_1 is generally compressive while σ_3 is generally tensile. We then extracted principal stress magnitudes over a regular 3D grid covering the entire arch lintel and abutments participating in support of the lintel (i.e. outlying regions of the abutments were ignored). All grid points located outside the arch volume were removed based on null stress values. The grid spacing for each arch varied with scale, such that the number of valid output values for σ_1 and σ_3 was approximately 75,000 (minimum 43k and maximum 116k points across all models; Table 1). The maximum grid spacing was 1 m at Rainbow Bridge (the largest overall arch) while the minimum grid spacing was 0.02 m at Rainbow Arch (the smallest arch). Most arches used consistent X,Y,Z grid spacing, however three sites with very thin lintels (e.g. Little Bridge) required anisotropic grids with smaller vertical spacing to accurately capture changing stresses across the lintel.

We quantified the distribution of the gridded principal stresses as histograms, showing the value of σ_1 and σ_3 spanning a common range of stresses from -0.5 to 2 MPa using 0.1 MPa bins. Bin counts were normalized as probability density function (PDF) estimates to account for differing numbers of stress elements for each arch and allow comparison between sites. The PDF was calculated as the number of elements in each bin divided by the product of bin width and total number of elements. We then computed the mean values of σ_1 and σ_3 for each site (Table 1), and calculated the mean principal stress ratio (MSR) as the absolute value of mean(σ_1) / mean(σ_3).

4. Results

Principal stress histograms for each arch are shown in Figure 4, where σ_3 values have been multiplied by -1 to allow overlay and comparison with σ_1. Negative σ_3 values in this case refer to nodes where σ_3 is compressive; these nodes commonly occur in arch abutment areas where larger bedrock overburden pressures generate compressive confinement. Comparing principal stresses across sites, two key results are apparent: 1) stress magnitudes are in general low and only a few sites have stresses exceeding the 2 MPa histogram cutoff (e.g. the longest arch, Landscape Arch; Figure 4g). Compressive stresses in particular are in all cases at least an order of magnitude lower than the reported compressive strengths for these materials (e.g. Moore et al., 2018). 2) Flat-lying arches with lintel geometries akin to a prismatic beam have nearly symmetrical σ_1 and σ_3 stress histograms (e.g. Two Bridge; Figure 4s). On the other hand, arches with greater convex curvature have predominantly compressive stress distributions (e.g. Causeway Arch; Figure 4b). Rainbow Bridge (Figure 4a), meanwhile, has a unique compressive stress distribution with a relatively small number of very low stress values, while relatively large tensile stresses result from the propensity of the arch to flex in the out-of-plane direction. Most arches have stress distributions skewed toward greater relative σ_1, indicating compressive stresses are dominant, but several exhibit significant tensile stresses.

Field observations confirm that areas of tensile stress predicted in our models frequently correspond to the locations of suspected tensile cracks. Figure 5 shows three examples where vertical open cracks observed in the field correspond to the locations of tensile stresses predicted from 3D gravitational stress models. In each of these cases, tensile stresses are located at the arch abutments as well as the center-underside of the lintel, as expected for a beam deforming under gravitational loading. Even in the case of Double O Arch with its curved underside, tensile stresses are still found at the arch center. The magnitudes of predicted tensile stresses vary in these cases from 0.5 MPa to 3 MPa; within the nominal range of tensile strengths for sandstones of this type (Goodman, 1989). Rainbow Arch, which collapsed in the winter of 2017-18, exhibited a large tensile crack visible on the middle-underside of the lintel, consistent with model predictions of peak tensile stresses in this area of ~0.15 MPa.

To summarize principal stress distributions across sites of varying scale and geometry, we calculated the mean principal stress ratio (MSR), with values shown in Figure 6 and Table 1. Results demonstrate that flat, beam-like arches (e.g. Two Bridge), with symmetrical compressive and tensile stress distributions, have MSR values close to 1, while arches with a flat top but curved underside (e.g. Owachomo Bridge) have slightly greater overall mean compressive stresses and higher MSR.

Arches with increasing lintel convexity have greater MSR (e.g. Landscape Arch) indicating stress distributions are more compressive and tensile stresses are reduced. At larger MSR values we find arches with highly curved lintel top and bottom surfaces and narrower openings (e.g. Delicate Arch). These arch forms naturally maximize compressive stresses and minimize tensile stresses, as reflected by the MSR. The greatest MSR value for all arches in this study was found at Rainbow Bridge (Figure 7), which has a lintel geometry that minimizes tensile stresses (see Figure 3g) while generating generally high compressive stresses (Figure 3e). This geometry closely resembles that of an inverted catenary and achieves the engineering goals of the form – reducing tensile stresses and holding the self-weight of the arch in compression (Handy, 1973). Figure 7 summarizes all MSR results shown together with simplified sketches of arch geometry, allowing visual comparison between MSR and arch form and confirming that arches with convex lintels have greater MSR while those with beam-like lintels have lower MSR.

5. Discussion

Calibrated eigenfrequency models served as the basis for this analysis, with measured structural dynamics used to constrain the geometry, boundary conditions, and material properties of each arch (Geimer et al., 2020). Assumptions of uniform material properties (density and Young's modulus) were also validated by eigenfrequency matching (Moore et al., 2018). A common problem with these models, however, occurs in cases with uncertain boundary extents. Moore et al. (2018) showed how selection of boundary extents can affect eigenfrequency results, and the same is true for our gravitational stress analysis. For freestanding arches (e.g. Delicate Arch), boundary conditions are clear, however natural arches often abut vertical walls where selection of boundaries can be challenging (e.g. Corona Arch; Figure 2e). Lateral boundaries must be kept wide enough to allow stress isosurfaces to extend into the abutments, but also constrained to exclude rock volumes not influenced by arch stresses. We found that positive (i.e. compressive) mean σ_3 values in our models indicated too much lateral or basal material had been included in the analyzed volume, and in the net, moving boundaries inward had the effect of lowering the mean stress ratio. Therefore, in cases like Corona Arch, trimming away lateral and basal material not supporting the weight of the arch was necessary.

Our finite-element models assume a connected elastic medium throughout and can thus produce unrealistic stress concentrations, e.g. at the edges of the models. In some models these stress concentrations could be avoided by placing the fixed boundaries far from lintel (e.g. Owachomo Bridge, Figure 3). This allowed stresses from the lintel to follow a natural trajectory through the arch abutments. In such models, we verified that the fixed model boundaries were not affecting the stresses in the lintel by creating stress isosurfaces and ensuring these did not interact with our boundaries. In cases where this could not be avoided (e.g. Rainbow Bridge), our finite-element models produced stress concentrations at the fixed boundaries. However, when our results are processed statistically, the influence of these stress concentrations is markedly reduced. That is, stress concentrations produce large values but only in small areas, so the total number of grid nodes affected is small and the impact on the overall stress distribution and mean stress calculation is minimal. On the other hand, our finite-element models cannot capture real stress concentrations that may exist, e.g. at open cracks, and in these cases may underestimate actual local stress magnitudes (see Figure 5). Out-of-plane (i.e. with respect to the plane of the opening) stresses also influence our results. For example, in the case of Rainbow Bridge, the arch is leaning outward giving it a propensity to topple, which is opposed by intact rock connection and tensile strength of the neighboring rock knoll.

For comparison with our results of real arch forms, we manually created two synthetic arch geometries and calculated gravitational stresses and MSR values using the same methodology as above. The first was a flat prismatic beam with rectangular cross-section and scale mimicking Two Bridge, while the second was an inverted catenary scaled after Rainbow Bridge, with analytical surfaces following an inverted hyperbolic cosine. As expected, the results for the flat beam produced symmetrical σ_1 and σ_3 spatial and statistical distributions, mirrored about a horizontal axis of symmetry, and an MSR of 1. The theoretical inverted catenary form, on the other hand, generated a very low mean σ_3 value and high mean σ_1 (i.e. tensile stresses were reduced to nearly zero throughout the volume and the self-weight was held almost entirely in compression), and the resulting MSR was 334. Note that a perfect inverted catenary form would have infinite MSR as mean tensile stresses drop to zero. In our imperfect model, adverse stress concentrations could not be avoided, nonetheless the MSR is a full order of magnitude greater than in real arch geometries studied.

The MSR metric used to evaluate gravitational stresses appears to adequately summarize the stress conditions in real rock arch forms. One benefit of the metric is that the use of mean principle stresses limits the effect of stress concentrations on the final result. Another benefit is that normalizing stresses as a ratio makes the resulting MSR independent of arch scale. This can be assessed by comparing Figures 4 and 7. While small arches have lower overall stress magnitudes, MSR normalizes across magnitudes to allow comparison of arches with spans varying from 4 to 88 m. The metric in turn shows general qualitative (Figure 7) and quantitative match (theoretical results described above) with real and synthetic arch forms. Another

benefit of the metric is that it can be calculated relatively easily, and thus potentially for a far larger number of sites than analyzed in this study. Creation of photogrammetric 3D models is increasingly practical, and even without eigenfrequency calibration, these models can be rapidly analyzed in a variety of simulation packages for calculation of gravitational stresses (density and modulus need only be assumed or measured). Using the methodology above, i.e. exporting principal stresses on a regular grid and post processing results simply as mean(σ_1) / mean(σ_3), a large number of arches could be assessed. Note that while Table 1 reports MSR to one decimal place for comparison, Figure 7 rounds these to integer values which may be more appropriate considering assumptions and possible sources of error (e.g. stress concentrations, boundary extents).

Our results show that while an inverted catenary form is an ideal theoretical geometry for a natural arch, minimizing tensile stresses, real rock arches rarely achieve this form and exist in geometries that may be less favorable for long-term stability. A flat beam form, for example, is common where horizontal resistant rock beds are exposed in a sedimentary sequence or at a caprock surface, but may be subject to quicker collapse due to large tensile stresses. Lintel forms that minimize tension and maximize compression, on the other hand, appear more frequently for freestanding arches in massive rock masses (i.e. few intervening discontinuities or weak layers), and as this form has few areas under tension, rock arches with catenary geometry may be more stable and achieve longer lifespans. Rates of arch formation and collapse are unfortunately poorly known, so at this time it is not possible to quantitatively relate arch geometry and longevity. However, we hypothesize that geometry plays a strong role in controlling the long-term stability of arches, and thus that the MSR metric shown here may be a qualitative indicator of arch stability under gravitational loading. Although the precise conditions of its failure are unknown, Rainbow Arch, which collapsed during the study period, had an MSR value of ~3.

6. Conclusions

Static stress conditions underpin the erosional evolution of rock arches. Gravitational stresses are in turn a function of arch geometry, and can be simulated using 3D numerical models. We performed a suite of 19 simulations for arches ranging in size from 4 to 88 m using geometries developed from ground- and drone-based photogrammetry, and with material properties previously calibrated from dynamic analysis of ambient vibrations. Our results show that principal stress magnitudes are generally low, with peak compressive stresses well below the uniaxial compressive strength of sandstones but peak tensile stresses approaching the range of common tensile strengths. Areas of predicted tension in our models frequently correspond to observed tensile cracks in the field. We evaluated principal stress histograms for each arch and found that lintels shaped similar to a flat beam have nearly symmetrical compressive and tensile stress distributions, while more convex forms shaped like an inverted catenary have lower relative tensile stresses. Because of the low tensile strength of rock, reduced tensile stresses may favor long-term stability. These comparisons were clarified by analysis of the mean principal stress ratio for each site and compared to theoretical results; for a theoretical flat prismatic beam the MSR is 1, while for an inverted catenary the MSR tends toward infinity. Our results highlight stress conditions in several arches that approach end-member cases (e.g. beam-like arches with MSR close to 1), and the spectrum of principal stress ratios produced by natural variation of real arch forms. This indicates the ability of arches to self-sculpt into ideal stress-based forms is commonly limited by rock mass structure, and natural arches frequently evolve with geometries producing high tensile stresses that may be less favorable for long-term stability. The mean principal stress ratio summarizes the stress conditions in an arch and is comparable across scales with limited sensitivity to outlier values, and may thus provide a useful metric to aid relative assessment of arch stability in support of hazard and conservation analyses.

Acknowledgements

This study was supported by the Canyonlands Natural History Association and by the National Science Foundation grant EAR-1831283 to Moore. We are grateful to Arches, Canyonlands, and Bryce Canyon National Parks, as well as Natural Bridges and Rainbow Bridge National Monuments for access to study sites. We thank Jack Wood and Eric Bilderback for sharing photogrammetry models and expertise, as well as Ben White, Ashley Russon, Ammon Hatch, Kathryn Vollinger, and Natan Richman for assistance with field data collection. We are grateful to Piotr Migoń and an anonymous reviewer for providing valuable suggestions that improved this manuscript. Several of the 3D models created for this study can be accessed at: https://doi.org/doi:10.7278/S50D-G31E-NFW2.

References

Blair, R. W., Jr. (1987). Development of natural sandstone arches in south-eastern Utah, in Gardiner, V., ed., International Geomorphology 1986: Manchester, U.K., University of Manchester, 597-604.

Bruthans, J., Soukup, J., Vaculikova, J., Filippi, M., Schweigstillova, J., Mayo, A.L., Masin, D., Kletetschka, G. and Rihosek, J. (2014). Sandstone landforms shaped by negative feedback between stress and erosion. Nature Geoscience, 597.

Castigliano A.P. (1879) Théorie de l'équilibre des systems élastiques. Turin: Negro, and Paris: Baudry.

Cruikshank, K.M., and Aydin, A. (1994). Role of fracture localization in arch formation, Arches National Park, Utah. Geological Society of America Bulletin, 106(7), 879-891.

Eppes, M. C., and R. Keanini (2017). Mechanical weathering and rock erosion by climate-dependent subcritical cracking, Rev. Geophys., 55, 470–508.

Filippi, M., Bruthans, J., Řihošek, J., Slavík, M., Adamovič, J., and Mašín, D. (2018). Arcades: Products of stress-controlled and discontinuity-related weathering. Earth-Science Reviews, 180, 159-184.

Geimer, P.R., R. Finnegan, and J.R. Moore (2020). Sparse Ambient Resonance Measurements Reveal Dynamic Properties of Freestanding Rock Arches. Geophysical Research Letters, 47, e2020GL087239, doi: 10.1029/2020GL087239.

Gerber, E., and Scheidegger, A. E. (1969). Stress-induced weathering of rock masses. Eclogae Geol. Helv., 62, 401-415.

Gere, J. M., and Timoshenko, S. P. (1997). Mechanics of materials, PWS Pub. Co., Boston, MA.

i Ginovart, J.L., Coll-Pla, S., Costa-Jover, A., and López Piquer, M. (2017). Hooke's Chain Theory and the Construction of Catenary Arches in Spain. International Journal of Architectural Heritage, 11(5), 703-716.

Goodman, R.E. (1989). Introduction to rock mechanics, Wiley, New York.

Greif, V., M. Brcek, J. Vlcko, Z. Varilova, and J. Zvelebil (2017). Thermomechanical behavior of Pravcicka Brana Rock Arch (Czech Republic). Landslides, 14(4), 1441-1455.

Handy, R.L. (1973). The igloo and the natural bridge as ultimate structures. Arctic, 26(4), 276-281.

Heyman, J. (1997). The stone skeleton: structural engineering of masonry architecture. Cambridge University Press.

Hibbeler, R. C. (1999), Structural Analysis, Fourth Edition, Prentice Hall, NJ.

Howard, A. D., Kochel, R. C., and Holt, H. E. (Eds.). (1988). Sapping features of the Colorado Plateau: A comparative planetary geology field guide (Vol. 491). Scientific and Technical Information Division, National Aeronautics and Space Administration.

Laity, J.E., and Malin, M.C. (1985). Sapping processes and the development of theater-headed valley networks on the Colorado Plateau. Geological Society of America Bulletin, 96(2), 203-217.

Leith, K., J.R. Moore, F. Amann, and S. Loew (2014). In Situ Stress Control on Micro-Crack Generation and Macroscopic Extensional Fracture in Exhuming Bedrock, Journal of Geophysical Research, 119, 1-22, doi: 10.1002/2012JB009801.

Moore, J.R., P.R. Geimer, R. Finnegan, and M.S. Thorne (2018). Use of Seismic Resonance Measurements to Determine the Elastic Modulus of Freestanding Rock Masses. Rock Mechanics and Rock Engineering, 51(12), 3937-3944.

Moore, J.R., M.S. Thorne, K.D. Koper, J.R. Wood, K. Goddard, R. Burlacu, S. Doyle, E. Stanfield, and B. White (2016). Anthropogenic Sources Stimulate Resonance of a Natural Rock Bridge. Geophysical Research Letters, 43(18), 9669-9676, doi: 10.1002/2016GL070088.

Ostanin, I., Safonov, A., and Oseledets, I. (2017). Natural erosion of sandstone as shape optimisation. Scientific reports, 7(1), 1-8.

Řihošek, J., Slavík, M., Bruthans, J., and Filippi, M. (2019). Evolution of natural rock arches: A realistic small-scale experiment. Geology, 47(1), 71-74.

Stevens, D. J., and McCarrick, J. E. (1988). The Arches of Arches National Park: A Comprehensive Study (Vol. 1). Mainstay Publishing, Moab, UT.

Viles, H. A. (2013). Linking weathering and rock slope instability: non-linear perspectives. Earth Surface Processes and Landforms, 38(1), 62-70.

Vařilová, Z., Přikryl, R., & Zvelebil, J. (2015). Factors and processes in deterioration of a sandstone rock form (Pravčická brána Arch, Bohemian Switzerland NP, Czech Republic). Zeitschrift für Geomorphologie, Supplementary Issues, 59(1), 81-101.

Table 1: Study sites; numbers refer to locations shown in Figure 1. Arch name, location, span, and host formation are indicated, as well as model Young's modulus, output grid spacing, and output grid count after removal of null values. Key results of numerical stress analysis included: mean σ_1, mean σ_3 (sign convention: compression positive, tension negative), and mean principal stress ratio (MSR).

#	Arch Name [a]	Location Lat., Lon. (decimal degrees)	Formation	Span (m)	Young's modulus (GPa)	Grid Spacing [b] (m)	Grid Count (x 10^3)	Mean σ_1 (MPa)	Mean σ_3 (MPa)	MSR
1	Aqueduct Arch	38.1372, -109.5167	Wingate	24	1.8	0.2	43	1.51E+05	-3.01E+04	5.0
2	Big Arrowhead	37.7396, -110.2708	Cedar Mesa	7	2.7	0.15	48	6.27E+04	-1.55E+04	4.0
3	Causeway Arch	37.8319, -109.6248	Navajo	11	1.0	0.3	62	1.58E+05	-6.46E+03	24.5
4	Corona Arch	38.5799, -109.6200	Entrada	34	3.5	0.4	55	3.09E+05	-3.07E+04	10.1
5	Delicate Arch*	38.7436, -109.4993	Entrada	10	8.0	0.2	63	1.46E+05	-9.12E+03	16.0
6	Double O Arch*	38.7991, -109.6211	Entrada	20	8.0	0.2	92	1.78E+05	-3.67E+04	4.8
7	Dutchman Arch*	38.8724, -110.7878	Navajo	9	12.5	0.4	104	1.90E+05	-4.88E+04	3.9
8	Ednah Natural Bridge	38.9858, -110.4298	Kayenta	9	3.0	0.2/0.05	74	8.04E+04	-6.98E+04	1.2
9	Landscape Arch	38.7907, -109.6072	Entrada	88	7.3	0.5	105	6.50E+05	-9.59E+04	6.8
10	Little Bridge Arch	38.4336, -109.6796	Cutler	11	3.0	0.15/0.05	64	1.00E+05	-9.46E+04	1.1
11	Longbow Arch	38.5423, -109.6128	Navajo	35	3.4	0.4	50	2.66E+05	-4.58E+04	5.8
12	Moonshine Arch	40.5561, -109.5461	Navajo	21	2.4	0.3	62	1.58E+05	-1.33E+04	11.9
13	Musselman Arch*	38.4359, -109.7698	White Rim	37	8.0	0.3	56	2.93E+05	-1.11E+05	2.6
14	Owachomo Bridge	37.5823, -110.0141	Cedar Mesa	55	8.0	0.5	96	2.87E+05	-8.44E+04	3.4
15	Rainbow Arch	38.6156, -109.6226	Entrada	4	2.0	0.04/0.02	51	3.94E+04	-1.15E+04	3.4
16	Rainbow Bridge	37.0774, -110.9643	Navajo	83	4.7	1.0	48	7.26E+05	-2.21E+04	32.9
17	Squint Arch	38.6465, -110.6739	Navajo	12	2.1	0.1	48	8.04E+04	-2.39E+04	3.4
18	Sunset Arch	37.3759, -111.0484	Navajo	18	2.3	0.2	57	1.16E+05	-1.57E+04	7.4
19	Two Bridge	37.6212, -112.1639	Claron	9	5.2	0.05	116	1.16E+05	-1.66E+05	0.7

[a] *Sites not included in Geimer et al. (2020) marked with asterisk*

[b] *Anisotropic grid spacing where indicated; second value refers to vertical spacing*

Figures

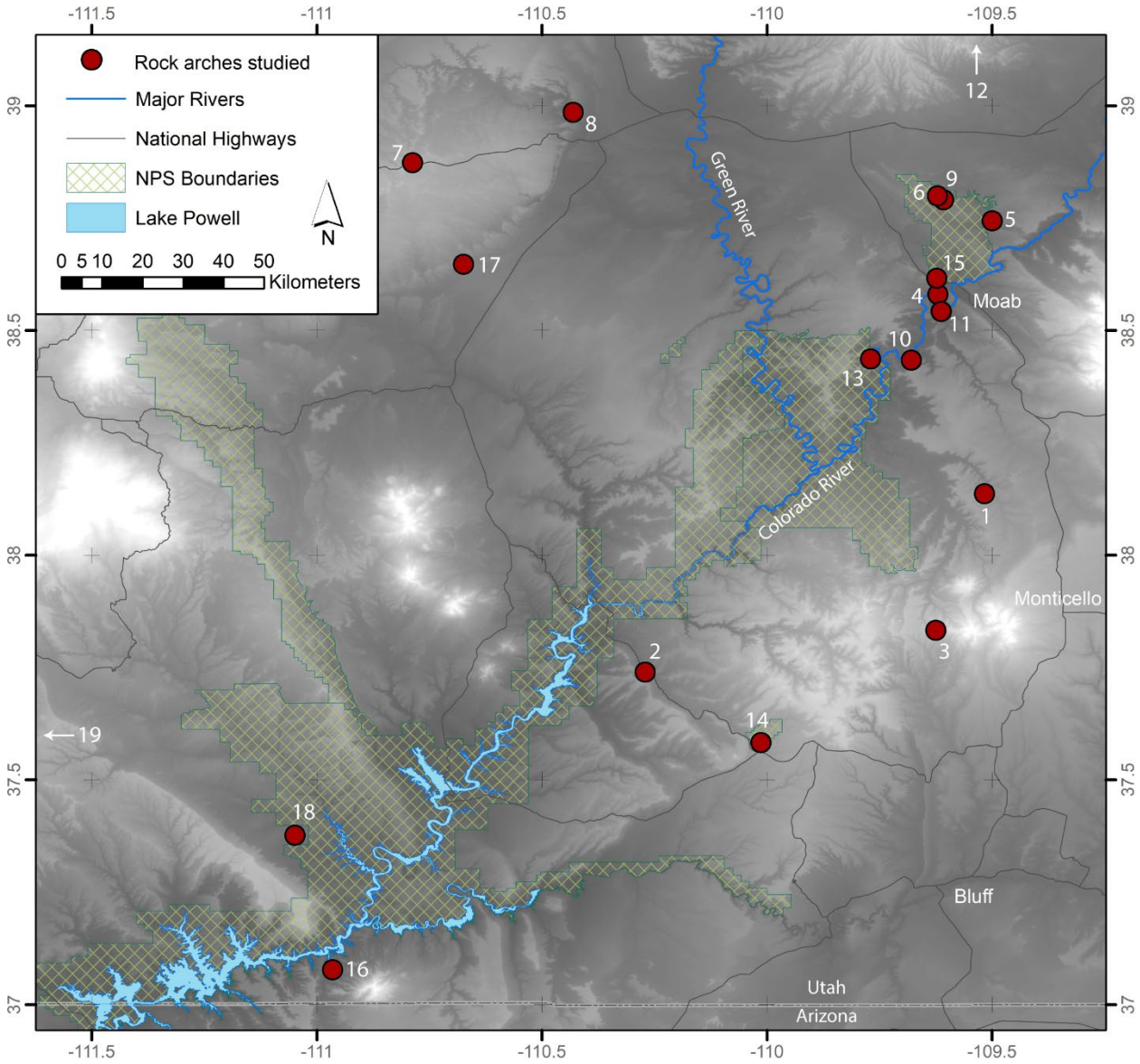

Figure 1: Location of arch study sites in southeast Utah. Numbers refer to sites in Table 1. Two arches are located off the map to the north and to the west. Select geographical features, National Park Service unit boundaries, and national highways are shown for reference.

Figure 2: Images of each arch. a)-s) show an oblique ground or drone based image of all arches analyzed in this study, with arch span indicated at lower right in each panel (see inset legend). Arches are arranged by decreasing mean principal stress ratio to facilitate comparisons to Figures 4 and 7.

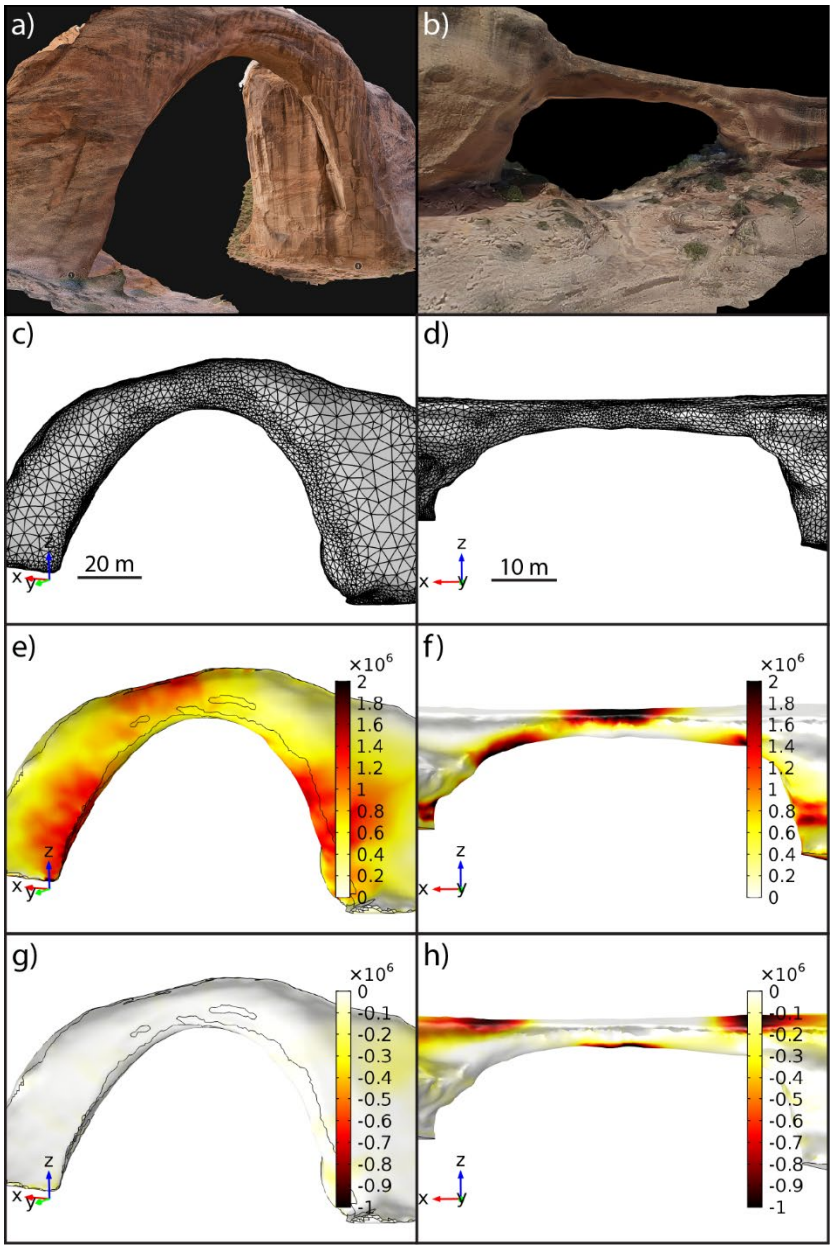

Figure 3: Example gravitational stress analysis for two arches (left: Rainbow Bridge; right: Owachomo Bridge. Panels a)-b) show views of the 3D surface models created from ground-based photogrammetry for these features, while c)-d) show the resulting finite-element mesh used for numerical analysis. Panels e)-f) show compressive principal stress magnitudes on the arch surface, while g)-h) show tensile stresses. Note strong differences in tensile stresses for Rainbow Bridge (g) versus Owachomo Bridge (h); the former being more like an inverted catenary has low overall tensile stresses, while the latter being more like a beam has high tensile stresses that mirror the compressive stress field.

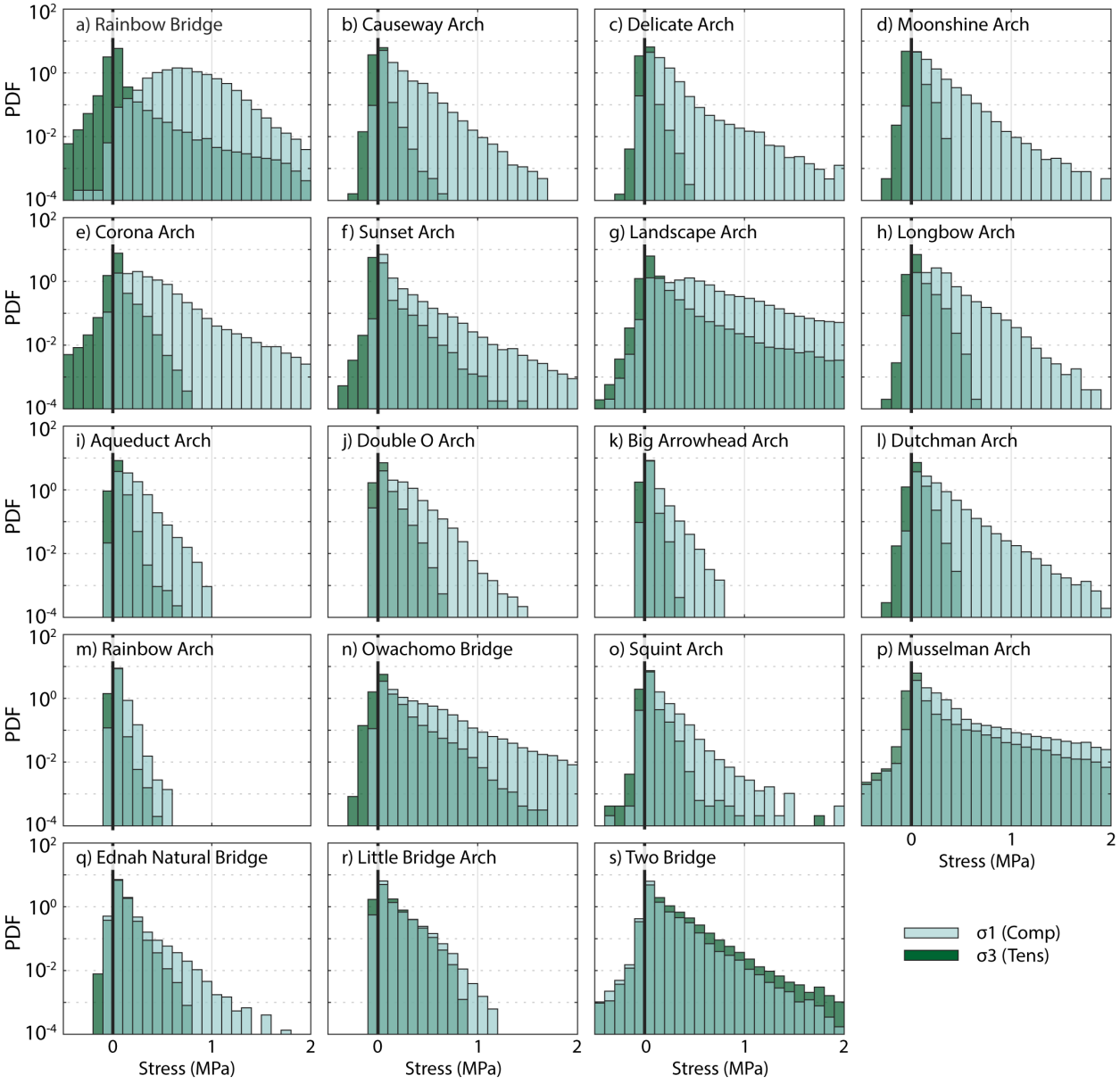

Figure 4: a)-s) Stress histograms for each arch (sites are ordered as in Figure 2). σ_3 values are multiplied by –1 to allow overlay and comparison with σ_1. Arches with beam-like geometry (e.g. Two Bridge) have more symmetrical σ_1 and σ_3 distributions, while those with greater convex curvature favor compressive stresses. Histograms use 0.1 MPa bins to display stresses between -0.5 and 2 MPa; bin counts are normalized as probability density function (PDF) estimates.

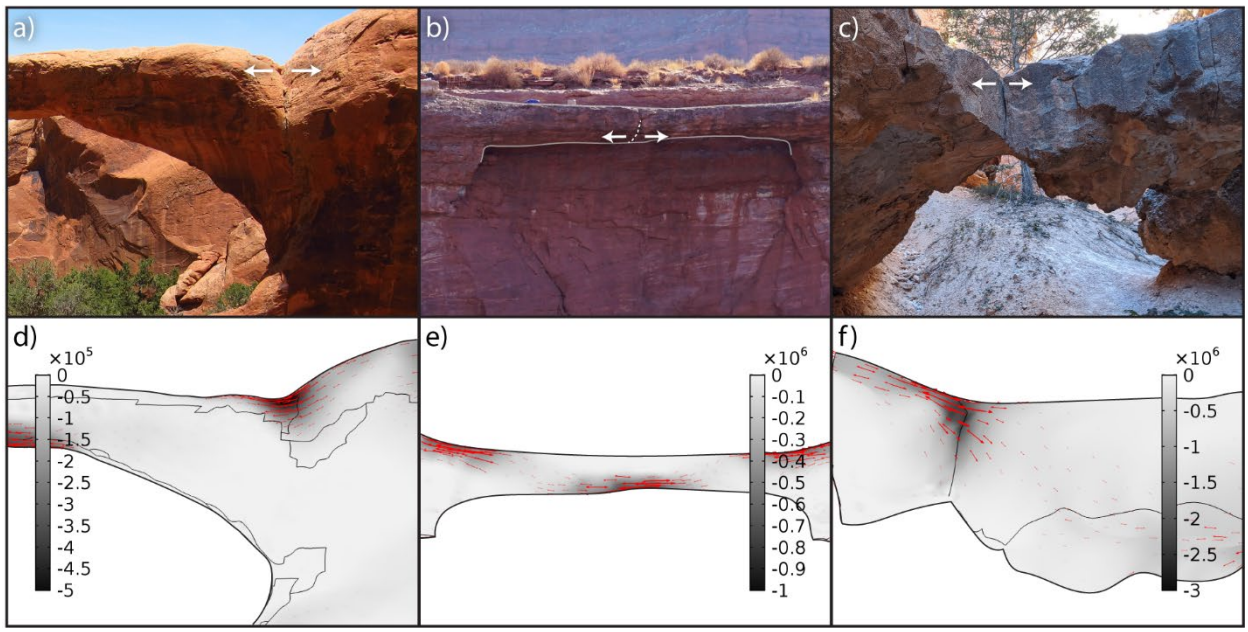

Figure 5: Cracks observed in the field corresponding to the locations of modeled tensile stress concentrations: Double O Arch (a,d); Little Bridge Arch (b,e), Two Bridge (c,f). Cracks are indicated on images with arrows showing the suspected orientation of tensile opening; crack trace is dashed in b) for clarity. Peak modeled tensile stresses range from -0.5 to -3 MPa, in the range of the tensile strength of most sandstones. Principle stress arrows indicate the orientation of tensile stresses. Note smoothing of the surface geometry in d) likely reduces the modeled peak tensile stress.

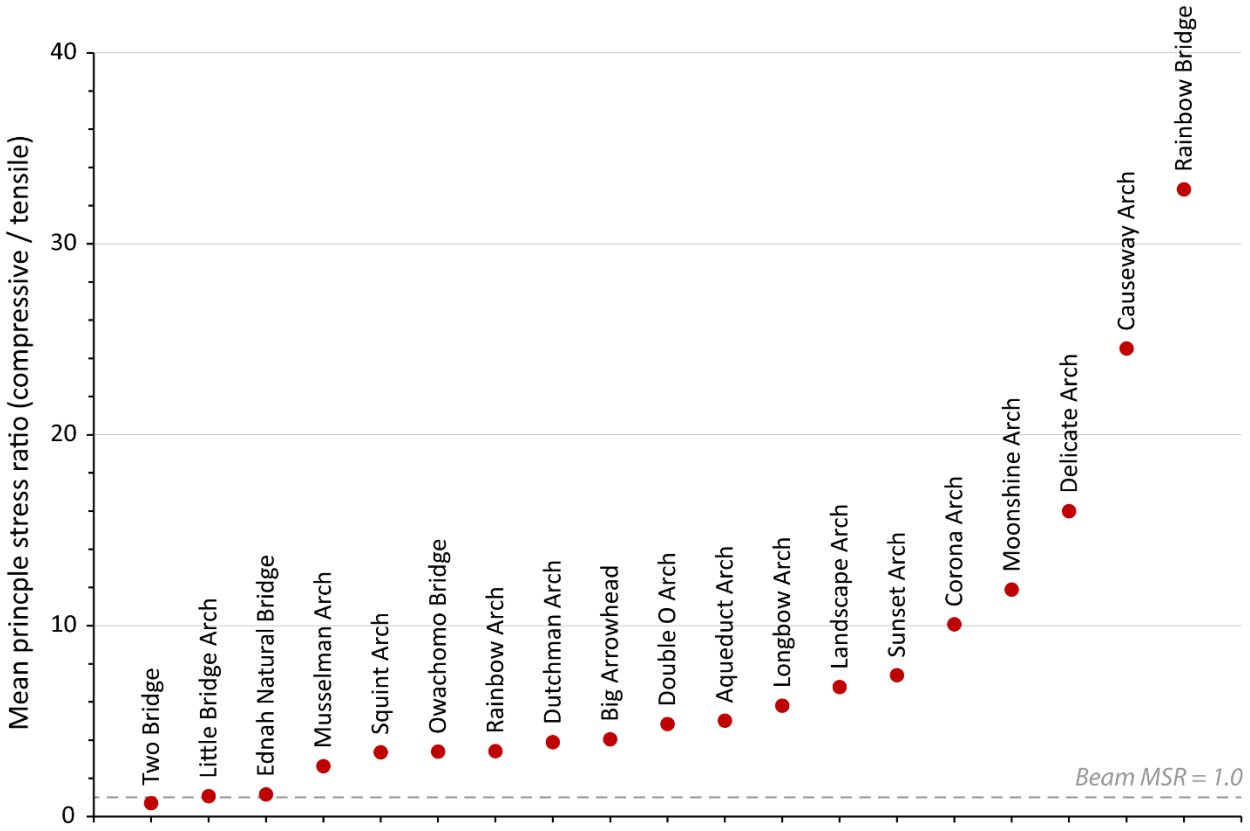

Figure 6: Mean principal stress ratio (MSR) for all arches in this study. Sites are arranged from lowest to highest MSR. Arches with flat, beam-like lintels have MSR close to 1, while those with increasingly convex curvature have greater MSR. At maximum, Rainbow Bridge has geometry that reduces tensile stresses throughout the lintel, akin to an inverted catenary, resulting in a high MSR value.

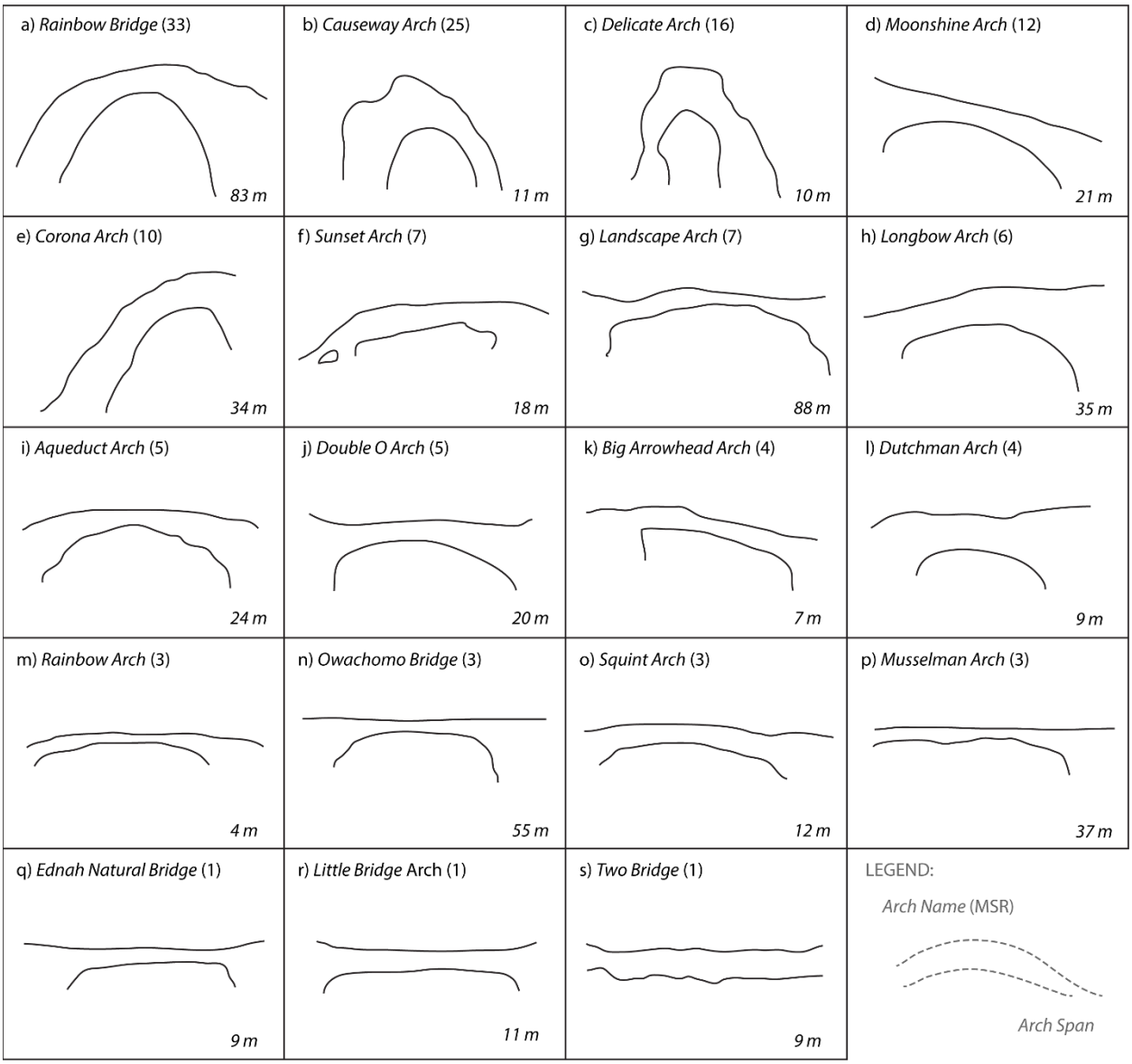

Figure 7: Comparison of mean principal stress ratio (MSR) with arch form. a)-s) show sketches of each arch (compare to photographs in Figure 2) with MSR value reported following the arch name and arch span at lower right (see inset legend).